Anti-icing properties of femtosecond laser-induced nano and multiscale topographies

Gaddam, Anvesh; Sharma, Himani; Karkantonis, Themistoklis; Dimov, Stefan

DOI:
10.1016/j.apsusc.2021.149443

Document Version
Peer reviewed version

Citation for published version (Harvard):
Gaddam, A, Sharma, H, Karkantonis, T & Dimov, S 2021, 'Anti-icing properties of femtosecond laser-induced nano and multiscale topographies', *Applied Surface Science*, vol. 552, 149443.
https://doi.org/10.1016/j.apsusc.2021.149443

Anti-icing properties of femtosecond laser-induced nano and multiscale topographies

Anvesh Gaddam[1], Himani Sharma[2], Themistoklis Karkantonis[1], Stefan Dimov[1]

[1]Department of Mechanical Engineering, School of Engineering, University of Birmingham, Birmingham B15 2TT, UK

[2]Department of Chemical and Biomolecular Engineering, University of Notre Dame, Notre Dame, IN 46556, USA

Abstract

Surfaces covered with micro, nano and multiscale topographies are the subject of significant interest due to their ice-repellency properties in the last decade. Ultrafast laser processing is becoming a widely used clean manufacturing technique to fabricate ordered nano and multiscale topographies on metallic surfaces over relatively large areas. In this work, single-tier nano and two-tier multiscale topographies were fabricated on stainless steel surfaces with one-step femtosecond laser processing to impart anti-icing response. Droplet freezing and frost formation on laser treated surfaces were examined at -10 ^{o}C and compared with the lubricant-impregnated and superhydrophobic nanoparticle-coated ones. While the hydrophilic nanoscale topography has accelerated the droplet freezing and performed worse than untreated surfaces, their hydrophobic counterparts increased the time to freezing by nearly two times. Overall, the superhydrophobic two-tier multiscale topography has significantly delayed both the droplet freezing time and frost formation on surfaces. Furthermore, the two-tier multiscale topography has sustained its anti-icing response even after being subjected to 25 abrasion cycles, while the surfaces with only nanoscale topography and nanoparticle-coating lost their functionality in only 10 cycles. Therefore, such robust two-tier multiscale topographies devoid of any coatings can enable and underpin many industrial applications where ice accumulation on surfaces results in performance degradation, e.g. in aerospace, refrigeration, air-conditioning and energy applications.

Keywords: Anti-icing, femtosecond laser, frost, LIPSS, stainless steel, superhydrophobic, textured surfaces, XPS.

1. Introduction

Ice accretion on metallic surfaces in engineering systems such as aircraft and wind turbine surfaces, pipelines in refrigeration and air-conditioning, and transmission power cables is a major concern as the ice build-up on surfaces could affect operational efficiency and, in some cases, leads to inadvertent system failures [1]. For instance, the formation of frost on the evaporators of refrigeration systems results in increased energy consumption [2]. Therefore, efforts to mitigate ice formation on metallic surfaces can reduce products' exploitation costs. The conventional de-icing methods based on mechanical, thermal, and chemical means, although effective are also energy- and resource-intensive and thus increase the operational costs [3-4]. On the other hand, the functionalization of surfaces by producing micro or nanoscale topographies is a passive method, which is gaining significant attention recently as a means for ice-repellence. Although the current state-of-the-art indicates that surface texturing promotes significant delays in ice formation and reduces adhesion, the main challenge is to fabricate cost-effectively textured surfaces containing micro, nano and multiscale topographies on engineering metals over large areas and 3D/free-form surfaces.

The anti-icing performance of textured surfaces is generally attributed to their low surface energy. Although the surface energy can be lowered to a certain extent by coatings that are composed of fluorinated compounds, they are not durable. Conversely, micro or nano topographies can reduce the surface energy to a greater extent depending on the treated material. Such low energy surfaces exhibit superhydrophobicity where water droplets in Cassie-Baxter state (CBS) are formed, especially due to the entrapped air in the micro or nano topographies. The attainment of CBS on textured surfaces when in contact with liquids was showed to impart benefits such as hydrodynamic drag reduction [5], anti-biofouling [6], and anti-wetting [7]. However, the transition of the metastable CBS to a stable Wenzel state (WS) leads to the loss of these functionalities. On the other hand, wettability is not a sole surface property that leads to ice repellence. Even if the textured surface exhibits higher water contact angles at room temperature, the local condensation in the interstitial spaces of micro topographies during the freezing conditions could still result in ice formation which is also referred as "Wenzel ice" [8]. Subsequently, the anti-icing functionality can only be achieved if textured surfaces sustain CBS under sub-zero temperatures [9]. One way to sustain CBS and thus achieve so called "Cassie ice" condition is through nano topographies, where the increased vapor pressure in the nanoscale cavities inhibit condensation. Such nano topographies or

multiscale topographies containing both micro and nano features have shown to exhibit higher anti-icing properties [10-11].

Fabrication of nano or multiscale topographies on metallic surfaces, therefore, is an important enabler for achieving anti-icing functionality in different industrial applications. Although lithography-based fabrication processes can produce periodic or random micro, nano and multiscale topographies for anti-icing applications, they are generally limited to silicon substrates and can be used only in a cleanroom environment [11-12]. At the same time, some cost-effective technologies for creating nano topographies with ice repellence properties, such as Zinc oxide (ZnO) [13-14], Carbon nanotube (CNT) [15], and Silicon dioxide (SiO_2) [16] coatings on metallic surfaces, have few drawbacks, especially base material selectivity and relative low durability. Another cost-effective approach to produce multiscale topographies for imparting anti-icing property on aluminum substrates is chemical etching followed by low energy coating [17-18]. Conversely, short and ultrashort pulse laser processing is environmentally friendly, non-contact and relatively easy to implement technology that is gaining significant attention as it can produce ordered nano and multiscale topographies on any material and thus to impart different functionalities.

Milles et al. [19] functionalized aluminum substrates with periodic multiscale topographies through nanosecond direct laser writing and laser interference patterning to impart anti-icing functionality. Long et al. [20-21] investigated random multiscale topographies that were fabricated on copper, aluminum, and titanium substrates with a nanosecond laser to achieve almost 50% delay in the frost formation on such textured surfaces. At the same time, Boinovich et al. [22] demonstrated long-term durable anti-icing properties on nanosecond laser treated aluminum alloy, however, fluorinated coatings were used, too, to achieve super hydrophobicity. Several investigations were focused on different implementations of ultrafast laser processing to increase its efficiency when imparting anti-icing functionality on aluminum substrates [23-24]. Recently, even a more cost-effective millisecond laser treatment was reported to demonstrate anti-icing functionality on copper surfaces [25]. Also, a comprehensive review dedicated to anti-icing applications of laser-treated surfaces was published recently that highlights the interdependences between that wettability, superhydrophobicity and anti-icing properties [26].

Although surface treatments with nanosecond lasers pave a way for cost effective fabrication of multiscale topographies, pico and femtosecond lasers are capable of producing both periodic

or random nano and multiscale topographies on almost all metallic surfaces in a reproducible and repeatable manner without any heat-induced negative side effects. Recently, anti-icing functionality of aluminum surfaces treated by a femtosecond laser is demonstrated [27-28]. However, the so-called laser-induced periodic surface structures (LIPSS) produced consistently employing femtosecond laser processing were showed to exhibit a variety of functionalities, i.e., anti-biofouling [29], anti-adhesion [30], and optical effects [31] by our group previously. Therefore, the fabrication of such LIPSS topographies on metallic surfaces could facilitate multifunctionality and thereby represent a value-adding treatment. Furthermore, since the single scale nano topographies are ideal for low ice adhesion [9, 32], it is worth understanding how LIPSS affect the freezing process. To this end, the main focus of this research is to investigate the freezing process on stainless steel substrates that underwent femtosecond laser treatments with single-tier nanometer length scale LIPSS and two-tier micro-nano length scale multiscale (MS) topographies. In particular, sessile drop-freezing and frost formation processes on such textured surfaces with different wettability were examined in order to assess their anti-icing functional response. Furthermore, in addition to pristine surfaces, we have also compared the anti-icing response of these textured surfaces in their pristine state and when impregnated with a lubricant were investigated and compared with that surfaces with a commercial superhydrophobic coating. When lubricant-impregnated surfaces (LIS) were studied, the issue of Cassie-Wenzel transition was circumvented by permeating the micro or nano topographies with an incompressible lubricant. Such surfaces facilitate condensation but in spite of this, they exhibited an anti-icing behavior due to the shedding of condensed droplets before being frozen [33].

2. Methodology

2.1 Fabrication of surface topographies

In this work, the AISI 430 stainless steel (SS) plates with dimensions 35 x 35 x 0.7 mm were used as substrates for femtosecond laser processing. The average surface roughness (S_a) of as-received SS plates was 40 nm. A micro-processing workstation (LS5, LASEA SA) was used to fabricate nano and MS topographies over an area of 30 x 30 mm on the SS plates (Fig. S1 of supplementary information). In brief, the system integrates an Ytterbium-doped laser source (Satsuma, Amplitude Systems) with average power of 5W, pulse duration of 310 fs, maximum pulse repetition rate of 500 kHz and wavelength of 1032 nm. The beam delivery sub-system incorporates a half wave plate to convert the beam into a linearly polarised one. The laser beam was steered with the 3D scan head and then focused to achieve a spot size of 35 μm by

employing 100 mm telecentric lens. The maximum achievable scan speed with the scan head was 2 m/s.

Two types of topographies, namely LIPSS and MS ones, were fabricated using this laser processing workstation. While the LIPSS surfaces have only single scale nanoripples, the two-tier MS surfaces were covered with micron-scale protrusions and nanoscale ripples again on top of them. In order to obtain these topographies, the processing windows determined in another research were used [29]. In brief, to fabricate LIPSS topographies, the laser beam was scanned on the surface at a speed of 1 m/s in a raster manner with a hatch distance of 4 μm and a fixed fluence per pulse of 210 mJ/cm^2. Regarding the MS topographies, a grid scanning strategy with a hatch distance of 35 μm in both directions, fluence per pulse of 415 mJ/cm^2 and a speed of 1 m/s was used. The surface chemical state of the laser processed substrates stored in ambient air is expected to alter with time and thus to influence their wetting properties [34]. Therefore, one set of the LIPSS substrates were kept in a water bath immediately after laser processing for 3 days to suppress surface chemical changes. While another set of LIPSS substrates were stored in ambient air. Hereafter, the LIPSS substrates that were stored in water were labelled as unaged LIPSS, while the ones stored in air were referred to as aged LIPSS.

Thereafter, to obtain LIS, a silicon oil (Sigma Aldrich) of 20 cSt viscosity was infused on one set of surfaces covered with the LIPSS topographies. Although, the lubricant could be infused on both LIPSS and MS topographies, it was previously shown that the lubricant-impregnated LIPSS topographies were durable under harsh conditions [30]. Finally, the plain SS surfaces were also coated with a commercially available state-of-the-art anti-icing NeverWet® (Rust-Oleum, Canada) coating to obtain another set of superhydrophobic surfaces. Hereafter, these nanoparticle coated surfaces are referred to as NW one. In total, the investigation of anti-icing functionality was conducted on six substrates with different topographies viz., plain, unaged LIPSS, aged LIPSS, MS, LIS and NW.

2.2 Characterizations

The surface topographies were first imaged by a scanning electron microscope (SEM, JEOL JCM-600). The dimensional measurements such as depth and periodicity of MS topographies were assessed by employing a focus variation microscope (Alicona G5). On the other hand, the depth and periodicity of the LIPSS topographies were analyzed by employing Atomic Force Microscopy (AFM, MFP-3D, Asylum Research). The X-ray Photon Spectroscopy (XPS, Kratos Axis Supra) was used to determine the surface chemical state of the plain, unaged LIPSS and aged LIPSS substrates. In particular, the XPS was conducted to verify the carbon

accumulation due to CO_2 decomposition from the atmosphere on unaged and aged LIPSS substrates after two weeks from the time of their laser processing. The measurements were conducted using a monochromatic Al Kα (1486.6 eV) over an analysis area of 300 x 700 μm^2. While the survey scans in the range of 0 – 1300 eV binding energy were recorded on the substrates with a pass energy of 160 eV, the narrow scans for high-resolution spectra of C1s and O1s were recorded with a pass energy of 40 eV. The obtained XPS spectra were analysed using the CasaXPS software. Thereafter, the wettability of all six substrates was analysed with a contact angle goniometer (OCA 15EC, Data Physics GmbH, Germany). Especially, the contact angle was investigated with 4 µl water droplets on all the functionalized surfaces every two days within two weeks. Whereas, the contact angle measurement on the unaged LIPSS was conducted immediately after laser processing and also after taking them out from the water storage, starting on fourth day after their removal.

The anti-icing behavior of all the five treated surfaces, i.e., unaged LIPSS, aged LIPSS, MS, LIS and NW, together with the pristine surfaces was examined inside custom-built insulated transparent chamber. The chamber was equipped with a Peltier element to obtain subzero temperature; aluminum water jacket and chiller to dissipate heat and maintain the substrate temperature; k-type thermocouples with a data acquisition system to record substrate temperature; and temperature and humidity sensors to monitor the chamber environment. In particular, the anti-icing tests were conducted at a constant temperature of -10 ^oC and relative humidity of 75% ± 3%. Side views of the sessile drop freezing, and frost growth processes on the substrates were captured using a digital microscope (Dino-Lite Premier, AM7013MT, 30 fps), while a top view of the frost formation process was recorded using a DSLR camera (Canon 2000D). In order to estimate the area covered by frost on the surfaces, the digital images were first converted into 16-bit grayscale ones using the ImageJ software. These grayscale images were further processed in this software by adjusting the threshold values and thus to differentiate between the frosted and unfrosted areas. The wettability and anti-icing measurements were conducted at least three times on all substrates to ensure their repeatability and also on three different sets for each treated surface to judge about their reproducibility.

3. Results and discussion

3.1 Surface morphology and wettability

In the first part of the research, the dimensional measurements were performed on the functionalized surfaces. Fig. 1 shows the SEM, AFM and 3D profilometer micrographs

together with the cross-sectional profiles of LIPSS, MS and NW topographies. As shown in Fig. 1 a, the LIPSS topography consists of closely packed quasi-periodic ripples with a periodicity of 800-900 nm. The LIPSS periodicity is approximately the same as the wavelength of the near-infrared (1032 nm) femtosecond laser used in the research. The AFM micrograph of the LIPSS topography is depicted in Fig. 1 a1. The corresponding cross-sectional profile in Fig. 1 a2 corroborates that the periodicity is in the range of 800 to 900 nm while their amplitude is between 100 nm to 200 nm.

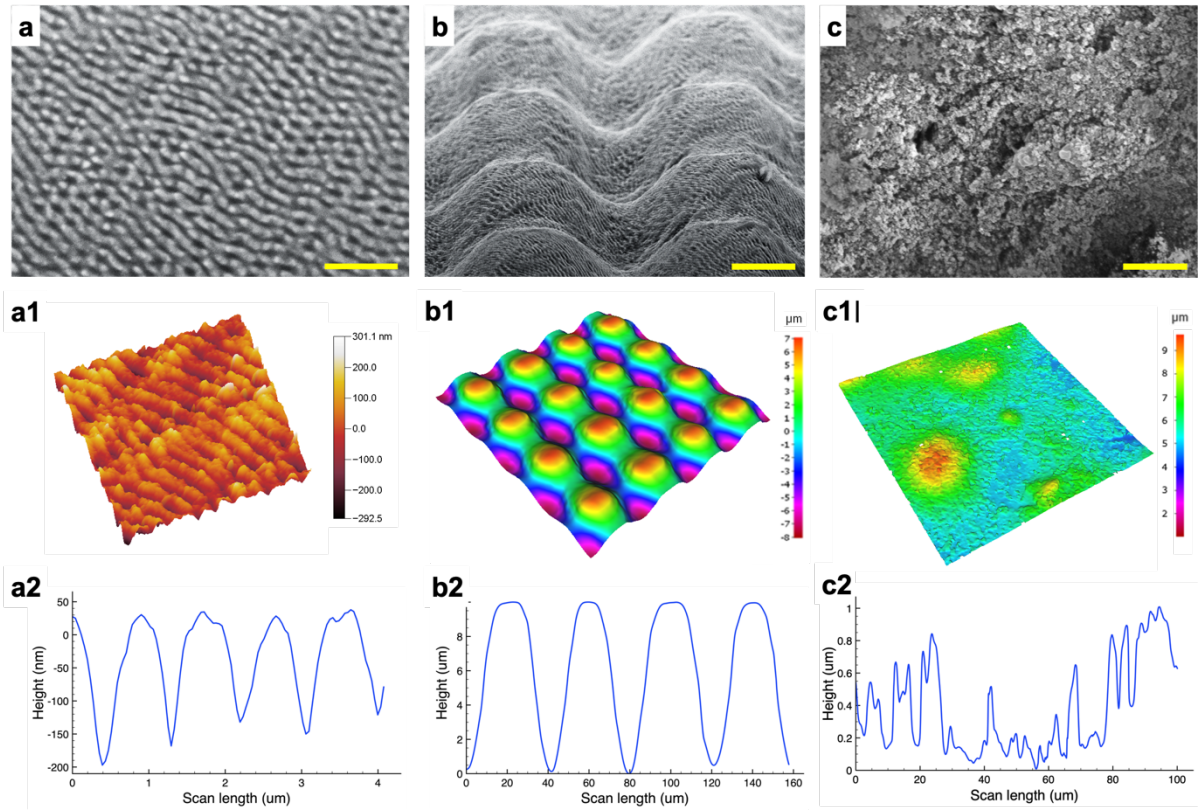

Figure 1: SEM, 3D AFM/profilometer micrographs with their corresponding cross-sectional profiles of **(a-a2)** LIPSS (scale bar: 5 µm). **(b-b2)** MS topographies (scale bar: 10 µm). **(c-c2)** NW coating (scale bar: 2 µm).

At the same time, the MS topographies consist of an array of micro-scale pillars with a periodicity of about 40 µm as shown in the SEM image in Fig. 1b. These pillars are in turn covered by nanoscale ripples which have a periodicity and amplitude roughly the same as LIPSS. The 3D data obtained with the Alicona profilometer and corresponding cross-sectional data plot in Fig. 1 b1-b2 indicates that the periodicity and height of the pillars are 40 µm and 10 µm, respectively. On the other hand, the NW topography has shown roughness at multiple

length scales from a few nanometres to few microns . The high-resolution SEM image in Fig. 1 c indicates that the coating indeed consists of nanoparticles clusters. It was previously shown that the average diameter of these superhydrophobic nanoparticles is around 20 nm [35]. The 3D height map and corresponding cross-sectional profile in Fig. 1 c1-c2 depict that the coating comprises of randomly distributed clumps of nanoparticles with a depth ranging from tens of nanometres to ten microns. As shown in Fig. S2 (supplementary information), the optical micrograph of the coating has revealed that the nanoparticles form clusters with diameters up to 30 μm at some locations and the coating contained cracks. S_a of the coating was measured to be 7.3 μm.

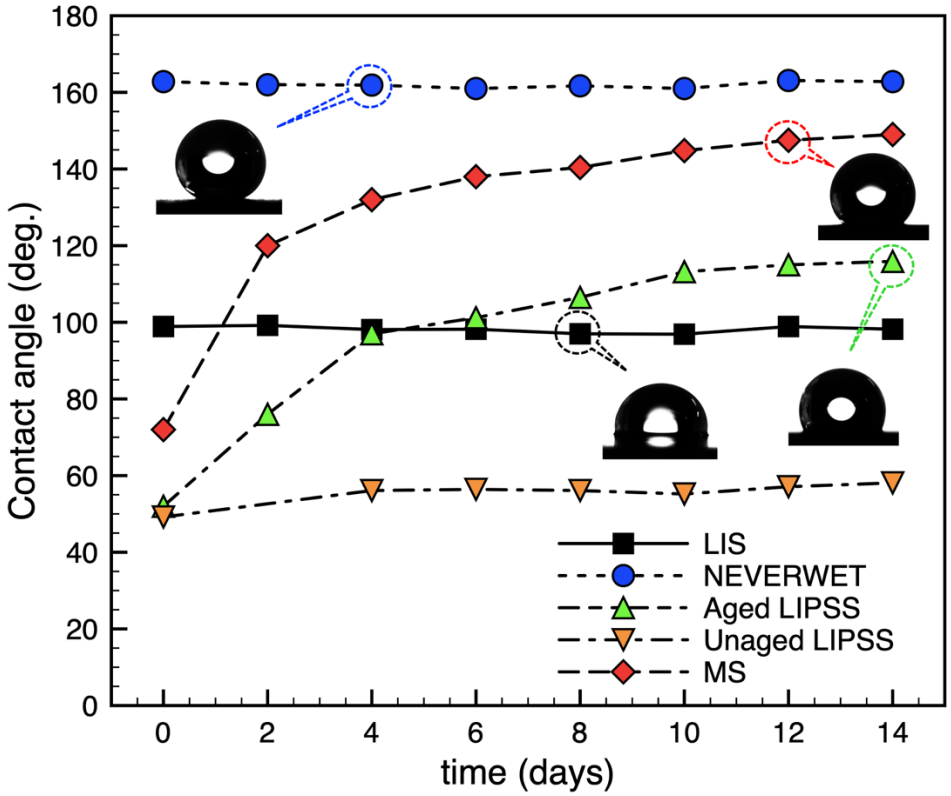

Figure 2: Contact angle as a function of time in number of days on five investigated topographies. The images of water droplet on respective surfaces are shown in the inset.

Next, the wettability of all the functionalized surfaces together with the pristine SS surfaces was analyzed over a period of two weeks. A water contact angle of 81° ± 2.8° was obtained on the pristine SS surfaces. Fig. 2 shows the variations of contact angles on LIS, NW, unaged LIPSS, aged LIPSS and MS surfaces as a function of time in days. The NW and LIS topographies have shown a stable water contact angle of 162° ± 1.5° and 98° ± 1.1°, respectively, over the two weeks and thus correspondingly they exhibited superhydrophobic

and hydrophobic properties. A contact angle of about 49° ± 1.8° on LIPSS topographies was obtained immediately after the laser processing. However, the contact angle on LIPSS topographies aged in ambient air, initially increased rapidly over a period of four days, and thereafter gradual over the two week they were analyzed. The contact angle of the aged LIPSS reached 115° ± 2.9° over the two weeks and thus they became hydrophobic. On the other hand, the unaged LIPSS stored initially in water for three days has shown a slight increase in the contact angle on the fourth day and then stabilized at 56.1° ± 3.2° within the following two weeks, hence exhibited hydrophilic properties. Similar to the aged LIPSS, the contact angle on MS topographies had increase rapidly, initially, and then gradually to reach 149° ± 2.9° within two weeks and thus to became almost superhydrophobic.

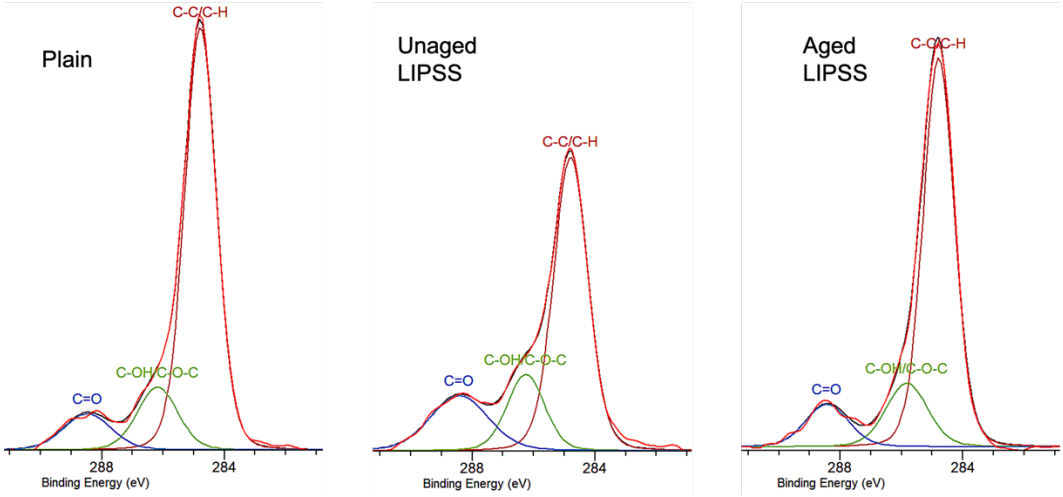

Figure 3: Normalized high-resolution C1s spectra of plain, unaged LIPSS and aged LIPSS.

The role of surface chemistry on wettability was investigated by conducting XPS measurements on the plain, unaged LIPSS and aged LIPSS samples. In particular, since the carbon accumulation was reported to influence the wettability over a period of time on laser processed metallic surfaces [36-37], the carbon enrichment of LIPSS topographies stored under different conditions was analysed and correlated to their respective contact angles. The chemical compositions were analysed by deconvolution of the C1 regions of the surveyed spectra of the plain, unaged and aged LIPSS as shown in Fig. 3. An increase in the signal corresponding to C-C/C-H can be observed for aged LIPSS when compared to the unaged ones at 284.7 ± 0.1 eV. Whereas the peaks corresponding to C-OH/C-O-C (288.4 ± 0.1 eV) and C=O (286.1 ± 0.2 eV) were noticed to be more intense in the case of unaged LIPSS. This indicates that the aging process in air has led to enrichment of the hydrocarbon species and reduced the content of the oxygenated carbon components. The relative magnitudes of C-C/C-

H, C-OH/C-O-C and C=O on reference plain, unaged and aged LIPSS surfaces are provided in Table-1. Since, the hydrocarbon compounds (C-C/C-H) are non-polar, their 10% increase on the aged LIPSS surfaces with respect to the unaged ones led to changes in wetting properties, i.e. surface hydrophobicity, and contact angles of 115°. On the other hand, a higher percentage of polar compounds (C-O-C, C=O) on unaged LIPSS has resulted into a lower water contact angle and thus led to a hydrophilic response.

Table-1: Percentage area of polar and non-polar carbon components on various surfaces obtained by fitting the C1s high resolution spectra.

	C-C/C-H (%)	**C-OH/C-O-C (%)**	**C=O (%)**
Plain	75.86	14.38	9.76
Unaged LIPSS	62.75	17.59	19.66
Aged LIPSS	72.96	16.05	10.98

At the same time, to achieve a stable Cassie-Baxter state, the magnitude of surface roughness should be more than the critical roughness factor, r_C (= $1/\cos\theta_E$), where θ_E is the equilibrium contact angle on a plain surface [38]. However, due to shallow undulations, LIPSS topographies exhibit a roughness factor less than r_C. Hence, the LIPSS topographies cannot exhibit a high contact angle unless the surface is aided by some accumulated non-polar hydrocarbons. Therefore, the unaged LIPSS topography with less content of the C-C/C-H exhibited hydrophilicity. It was reported that the accumulation of hydrocarbon compounds on LIPSS surfaces, when storing them in air for a sufficiently long period, led to super hydrophobicity [39]. However, since the LIPSS surfaces were stored in air only for two weeks in this research, the water contact angle increased only up to 115°.

3.2 Droplet freezing on surfaces

The water droplet freezing phenomenon was investigated to understand the anti-icing behavior of functionalized surfaces. In general, the freezing of a water droplet on any surface is categorized into different stages. When a water droplet is deposited on a sub-cooled surface, first, it assumes a shape depended on its wettability. Then, a decrease of the water contact angle follows as condensation is initiated on the surface. In the second stage, partial solidification commences, where the droplet consists of a mixture of water and ice. Afterwards, the solid-liquid interface propagates, staring from the bottom of the droplet, as part of the isothermal freezing stage as shown in Fig. 4a. The isothermal freezing of water droplets on MS and NW

surfaces are also shown in supplementary videos (S1). Finally, the freezing singularity occurs where the droplet assumes the shape of an ice cone. Fig. 4b depicts all stages of the droplet freezing process on unaged/hydrophilic LIPSS, aged/hydrophobic LIPSS, LIS, MS, and NW surfaces along with the reference/plain surface.

(a)

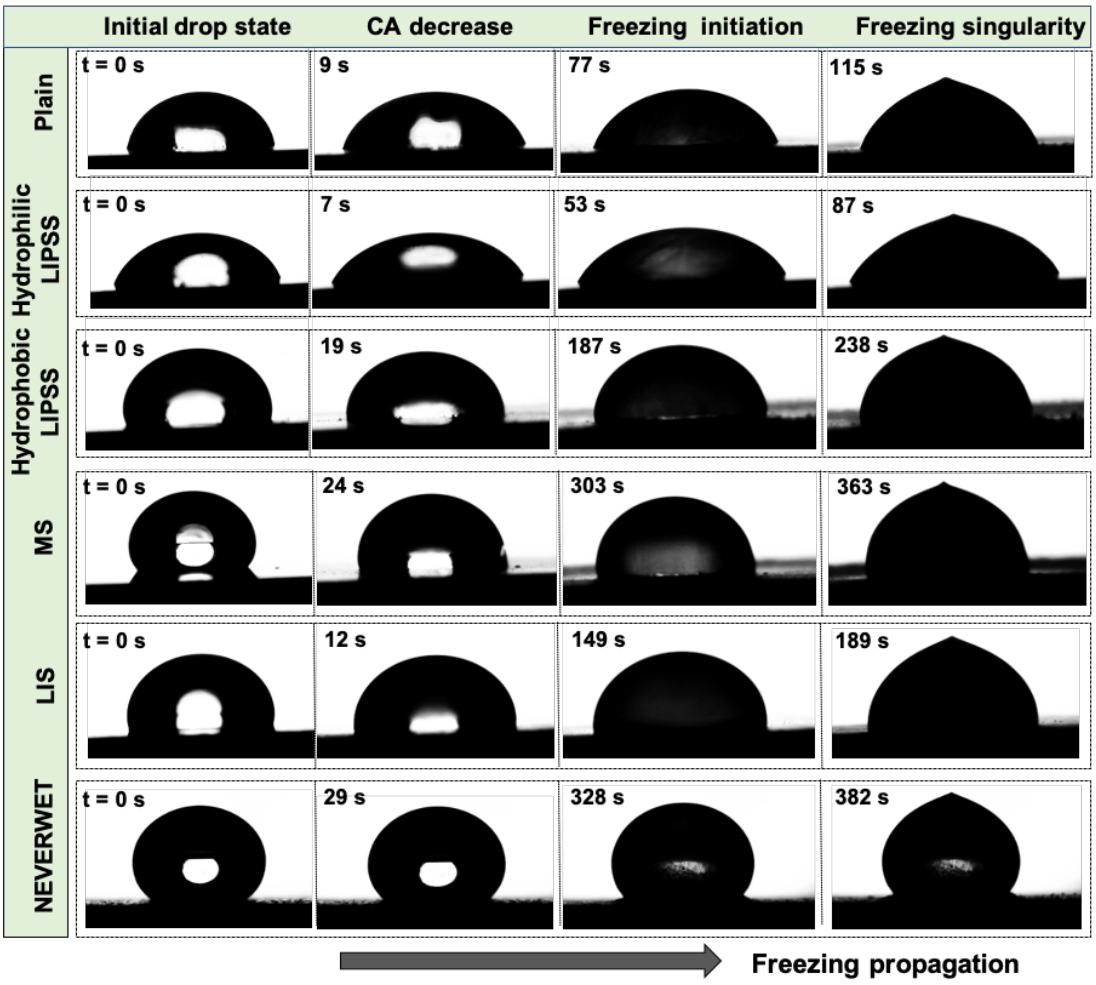

(b)

Figure 4: a. Isothermal freezing of droplet on a surface with MS topographies. **b.** Stages of sessile droplet freezing on all functionalized surfaces together with the reference/plain one.

On the plain surface, once the contact angle decreased to 63°, the partial solidification went for about 77s before the complete solidification occurred. The freezing singularity was reached in

less than two minutes on the plain surfaces. The hydrophilic nanoripples or the unaged LIPSS topography led to a decrease of the complete solidification time when compared to the plain surface. The increase of the effective contact area between the droplet and the surface due to the completely wetted Wenzel state could explain the enhanced heat conduction at the solid-water interface. Consequently, the droplet solidification is initiated quicker on the hydrophilic LIPSS topography, while on the hydrophobic LIPSS one, the droplet first assumes the Cassie-Baxter state that delays the solidification process. Once the freezing starts, condensate microdroplets surround the droplet. This results in a decrease of the water contact angle of the droplet to 87°. However, the nanocavities on the hydrophobic LIPSS surface tend to resist the complete wetting by the droplet due to the high capillary pressure [40]. So, the air pockets in the nanocavities reduce the effective contact area of the droplet with the surface and therefore the hydrophobic LIPSS have prolonged the initiation of solidification time by 110s when compared to the plain surface. Overall, the time required for the formation of an ice cone was doubled in the case of hydrophobic LIPSS when compared to the results obtained on the plain surface.

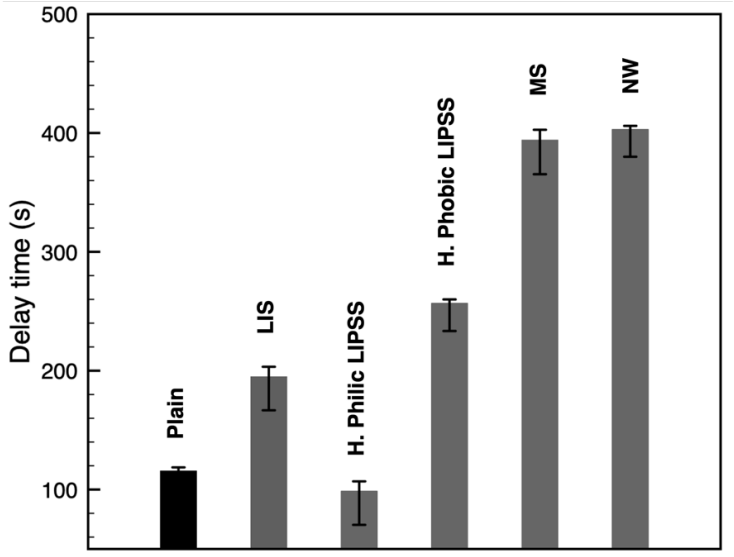

Figure 5: Freezing delay time of sessile droplets on investigated topographies together with the results obtained on the reference/plain surface.

The lubricant impregnation of LIPSS topographies (LIS) did not show any advantage in regard to their anti-icing response as shown in Figure 4b. Although the surface temperature was maintained at -10 °C, which was well below the freezing point of the silicon oil, the droplet solidified earlier on LIS than on the aged LIPSS surface. This could be attributed to the slightly

enhanced condensation on LIS than on the aged LIPSS surface. In the case of the MS topography, the reduction of the water contact angle was gradual and lasted for about 24s. The condensation during the cooling process leads to the formation of micro droplets on the interstitial spaces of the MS topography as shown in Fig. S3 of the supplementary information. These condensate droplets allow the droplet to transit from Cassie-Baxter to Wenzel state [41]. Due to this condensation-driven wetting transition into the deep microscale cavities, the contact angle decreased from 131° to 92.5°. However, similarly to hydrophobic LIPSS, the nanocavities present in the MS topography ensure a high capillary pressure and thus resist the complete wetting by the droplet. Therefore, the droplet's effective contact area with the surface is minimized by the nanoripples and this leads to a decrease of the heat conduction efficiency. Consequently, it has taken about 303s for the solidification to initiate on the MS topography. The magnitude of the contact angle decrease on the NW surface was however not drastic. This is because the NW coating has smaller sized microscale roughness than the MS topography. At the same time, the solidification time was marginally higher than that achieved on the MS topography.

The anti-icing performance of all functionalized surfaces is summarized in Fig. 5. As can be seen, the hydrophobic LIPSS and MS topographies led to more than 100% and 200% delay in freezing time of sessile droplet respectively, when compared to the results obtained on the plain surfaces. Overall, the NW surface has shown a better anti-icing performance than all other functionalized surfaces while the effectiveness achieved on the MS topography was almost the same. Conversely, the hydrophilic LIPSS topography led to a decrease of the anti-icing performance while the icing delay on LIS increased by about 50% when compared to the results obtained on the plain surface.

3.3 Frost growth and coverage on surfaces

The degree of frost formation on surfaces is another important anti-icing characteristic in addition to the delay in sessile drop freezing. Therefore, the frost formation on all functionalized surfaces under a similar substrate temperature and humidity conditions was investigated, too. The frosting on surfaces again can be categorized into distinct stages as depicted in Fig. 6. In the first stage, the condensation occurs in the form of nucleation and micro-droplets form due to coalescence on a cold surface. This is followed by a phase change process where the coalesced large droplets exhibit freezing singularities. Further, with time, the first frost branches appear on the cone of frozen droplets, which then grow into three-dimensional columnar structures. However, due to the gravity and surrounding conditions,

these structures quickly dislodge and become a frost layer. In the last stage, the new frost branches form on the underlying frost layer. In this research, top and side views of the frost formations on all functionalized surfaces were captured. In the side views, the frost thickness was observed to increase gradually in the initial 8 to 12 minutes and then the growth was rapid on all surfaces, similar to what was previously reported [42]. The final thickness of the frost was measured to be in the range from 1.1 to 1.3 mm on all surfaces.

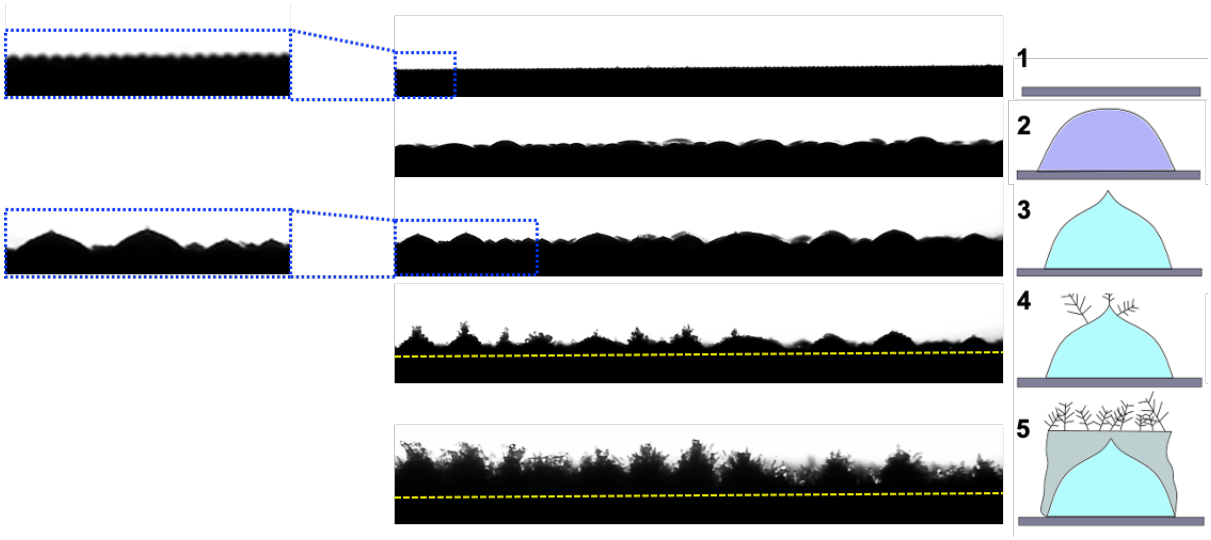

Figure 6: Stages of frost growth on a surface covered with MS topographies. (1) A bare surface. The inset shows micron sized bumps on the surface. (2) A formation of the condensed droplets. (3) Freezing of the condensed droplets. The inset shows freezing singularity of the individual droplets. (4) The formation of frost branches on the frozen droplets. (5) The growth of the frost branches on the frost layer. The yellow dotted line indicates the surface of the SS plate above which the frost had grown.

Fig. 7a shows the frost formation as a function of time on all functionalized surfaces together with the reference/plain one. Fig. 7b shows the percentage of the samples' area covered by the frost over a period of 50 minutes that corresponds to the top views shown in Fig. 7. As can be seen, the plain surface was covered with frost within 5 minutes from the start of the freezing process. After 20 mins, 90% of the surface area was covered with frost. The frost was observed to grow rapidly, initially, before reaching a plateau after 30 mins on the plain surfaces. The frost on hydrophobic LIPSS topographies has grown gradually and exhibited a quasi-linear growth pattern. Compared to the plain surface where the frost has taken only 6 minutes to form over 50% of the surface area, the LIPSS topography delayed the frost formation fivefold, approximately 30 minutes longer. However, once a sufficient number of micro-ice cones were formed on the surface, the frost growth occurred spontaneously. Therefore, the surface with

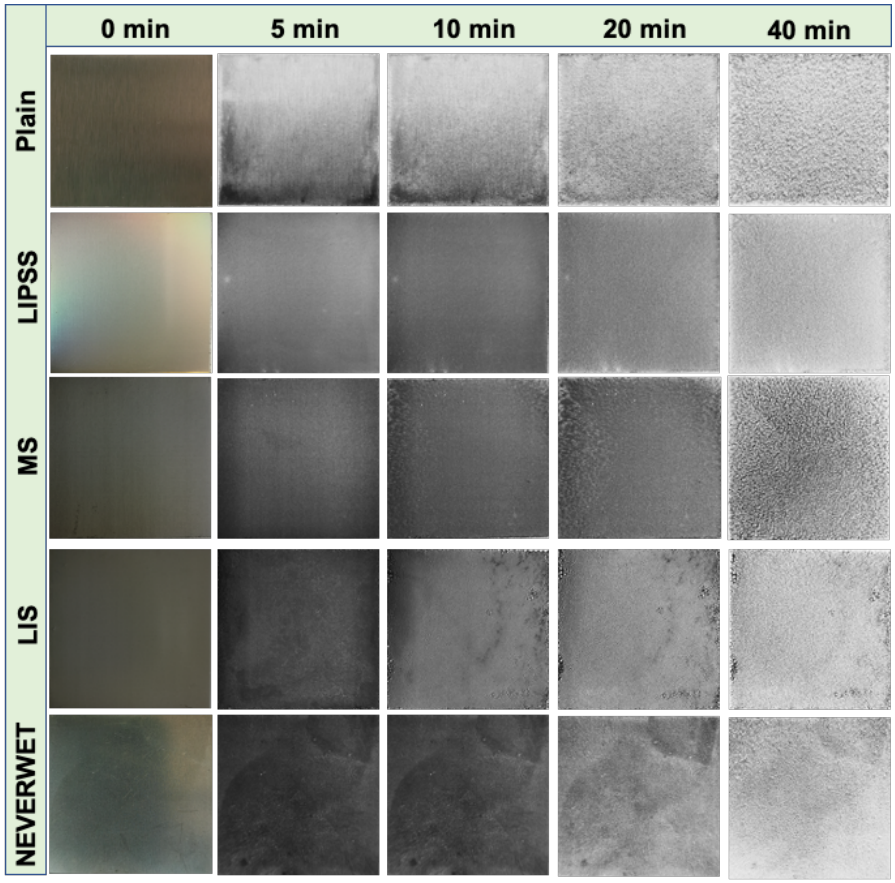

(a)

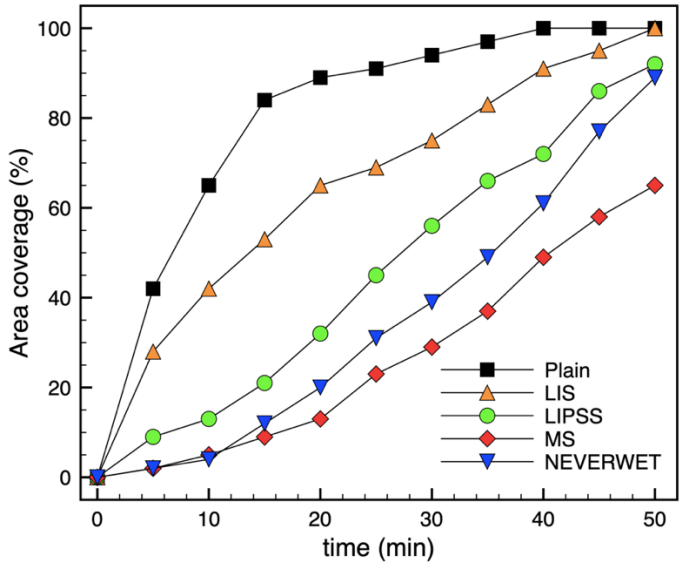

(b)

Figure 7: a. Images showing frost formation dynamics on functionalized surfaces compared with the reference/plain one (25 mm x 25 mm). Note: While the first column of the matrix shows true-color images of the functionalized surfaces, the rest of the matrix shows grayscale images to clearly show the frost coverage. Also, the light diffraction due to LIPSS topographies on the surface is clearly visible at the start of the freezing process. **b.** The areas covered by frost in percentages as a function of time on the reference/plain and functionalized surfaces.

LIPSS topography was almost fully covered by the frost within 40 mins. The frost formation on the LIS surfaces showed a similar growth pattern to that of the plain surfaces. This could be attributed to the enhanced formation of large micro-droplets on LIS due to the excellent mobility of nano-sized droplets on the smooth lubricant layer [43]. At the same time, the frost formation on LIS was delayed nearly twofold before it covered 50% of surface area when compared to the plain surfaces.

On the other hand, the frost formation on the surfaces with the MS topography was limited to only 10% of their area in the first 20 minutes. The NW topography showed a similar trend in regard to the frost growth to that of the MS topography in the first 10 minutes. However, the growth pattern on the former diverged after 15 minutes, especially the growth continued to increase on the NW topography. The superhydrophobic nanoscale features on top of the micro topography helped in avoiding the wetting transition of the condensed micro-droplets. When such micro-droplets coalesce, the larger droplets tend to jump out as excess surface energy transforms into kinetic energy. Therefore, coalescence-induced self-propelled droplets aid in sweeping the condensates and the frost formation is delayed on highly non-wettable nanoscale features of hierarchical topographies [17, 44]. It is expected that this response is a key characteristic of MS and NW topographies that delays the frost formation as shown in Fig. S4 (supplementary information). The jumping droplets on the two-tier MS topographies are shown in Video S2 of the supplementary information. However, unlike the two-tier MS topography, due to the multiple length scales of the roughness on NW topographies, the micro-droplets could have undergone the wetting transition at random locations (see Fig. S4 b). Consequently, the suppression of out-of-plane jumping when compared to the two-tier MS topographies is possibly reduced and this affects the anti-icing performance of the NW surfaces. Overall, only approximately 60% of the MS surface area was covered by frost in 50 minutes.

3.4 Durability of anti-icing surface response

The treated surfaces should be sufficiently durable to withstand a variety of abrasive/cleaning actions in order to retain their anti-icing functionality and thus to minimize their exploitation and maintenance costs in any given application. In particular, LIS surfaces were reported to fail in anti-icing applications due to the lubricant depletion while droplets freeze [45], whereas gas-cushioned textured surfaces lose their functionality because of wear and the worn roughness. Therefore, the anti-icing service life of the gas-cushioned textured surfaces in this research, i.e., LIPSS, MS and NW surfaces, was investigated when undergoing a mechanical

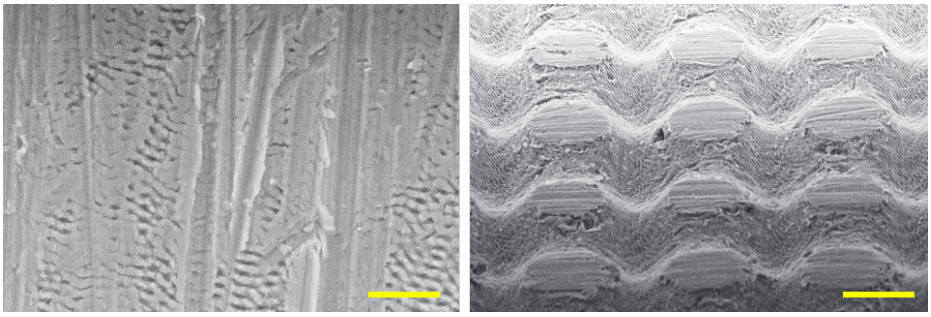

(a) (b)

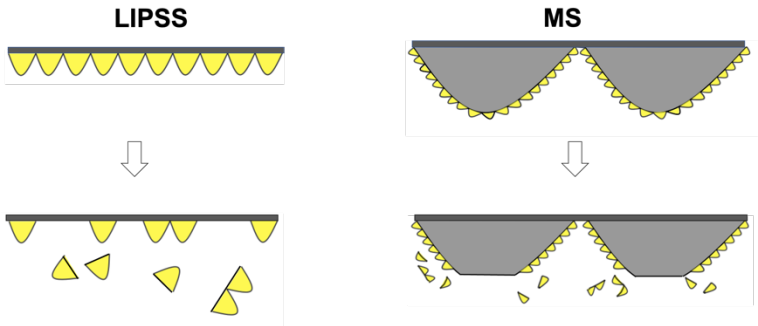

(c)

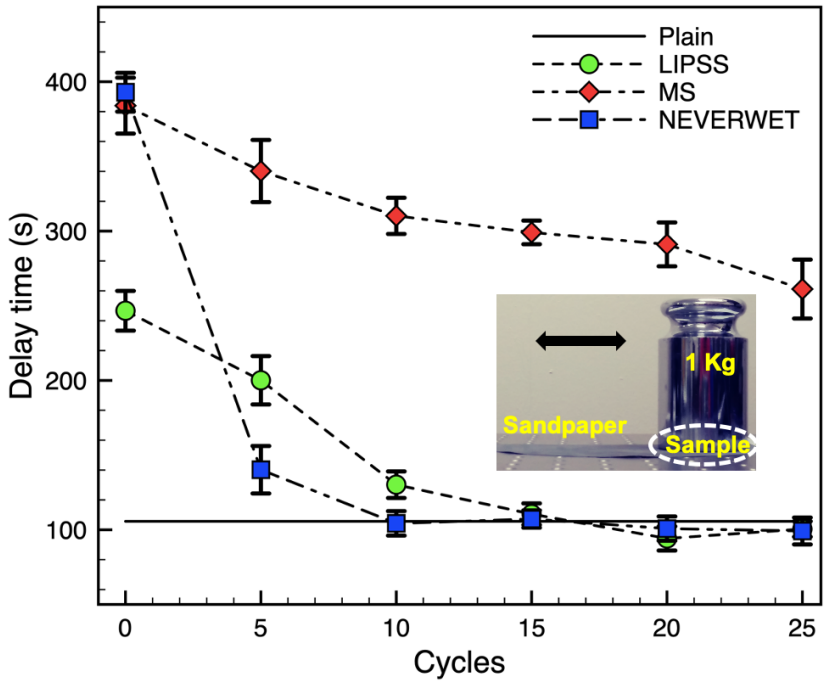

(d)

Figure 8: SEM micrographs showing **a.** LIPSS after 10 abrasion cycles (scale bar: 5 μm). **b.** MS topographies after 25 cycles (scale bar: 20 μm). **c.** An illustration showing the removal of nanoscale features from the LIPSS and MS topographies after abrasion cycles. **d.** The delay of the sessile droplets' freezing on different topographies compared with the reference/plain surface. The inset shows the set-up used for conducting the abrasion tests.

abrasion. In particular, the surfaces underwent abrasion cycles with a sandpaper (grit no. 600) under a weight of 1 kg (see Fig. 8d inset) over a stroke length of 150 mm.

The sessile drop freezing characterization was conducted after every 5 cycles on all three investigated surfaces. As shown in Fig. 8a, the nano-scale ripples were almost completely abraded after only 10 cycles. Whereas most of the ripples on MS topographies remained almost intact even after 25 cycles due to their protection by the microscale pillars that were worn as shown in Fig. 8b. The corresponding illustration in Fig. 8c depicts the result of the underwent mechanical abrasion and the removal of nano-scale ripples on MS topographies. Fig. 8d shows the delay of the sessile droplets' freezing as a function of increasing abrasion cycles on the three functionalized surfaces. As can be seen, the delay is reduced dramatically with each cycle on the LIPSS and NW topographies. Also, both topographies lost their anti-icing response within only 10 abrasion cycles. At the same time, the freezing delay is reduced gradually with the increasing number of abrasion cycles on the MS topographies. Even after 25 cycles, the freezing delay is nearly 2.5 times longer than that on the reference/plain surfaces. As evident from the SEM images, the nano-scale ripples remained on the MS topographies after the abrasion cycles as they were protected by the micro-scale protrusions and thus delayed further the loss of their anti-acing functionality.

4. Conclusions

Ultrafast laser processing has made significant advances in the last decade and is becoming a viable technology for fabricating multi-scale topographies over relatively large areas. Moreover, the laser processing not only produces periodic surface structures but also affects the surface chemical state and thus the wetting properties of surfaces can be tailored. Therefore, the ultrafast laser functionalization has attracted a lot of attention, both from industry and research, as it can offer an eco-friendly alternative to fluorinated coatings that are commonly used for functionalizing surfaces. The fabrication of such tailored topographies on metallic surfaces also opens the possibilities for designing passive anti-icing surfaces.

In this research, the anti-icing behavior of femtosecond laser-induced single-tier nanoripples (LIPSS) and two-tier multiscale (MS) topographies on stainless steel substrates were investigated. The functional response was compared with that of lubricant-impregnated and commercial nanoparticle-coated superhydrophobic surfaces. The six surfaces investigated in our research were crusted into three groups. In the first group, pristine and LIS surfaces had unstructured smooth surfaces with different wettability. The second group contained single-

tier nanostructures (LIPSS) with hydrophilic and hydrophobic properties. While the third group had two-tier micro-nano topographies and as a reference nanoparticle-coated multiscale structures exhibiting superhydrophobicity.

Overall, the surfaces with two-tier MS structures delayed significantly the droplet freezing time and suppressed frost formation compared with all other functionalized surfaces. Moreover, the two-tier MS topographies retained reasonably good anti-icing properties even after long abrasion cycles while this was not the cased with other alternative surface treatments. It was evident that the nanoscale ripples on top of the microscale protrusions provided increased stability against condensation-induced wetting transition, especially through the 'jumping droplet' effect on MS topographies. At the same time, the periodic and random nanostructures such as LIPSS and NW performed respectively better than the LIS samples. However, the anti-icing properties of such single nanoscale surface topographies were short-lived when the substrates were subjected to abrasion. Thus, the use of relatively easy to apply and commercially available icephobic coatings increases maintenance costs due to their poor durability. Furthermore, the likeliness of nanoparticles to cause a considerable harm to human health is another negative side effect also of these coatings [46]. Therefore, the durable laser-induced MS topographies could be a potential viable alternative. The MS topographies investigated in this research are simply an array of microscale protrusions and consist nanoscale ripples on top of them. In addition, as the ripples are the side effect of ultrafast laser pulse interactions with matter, the MS topographies with different designs, e.g. an array of trenches and/or dimples, could be produced relatively easily on metal substrates with ultrafast laser sources. Rational design of such tailored topographies can pave a way for improving anti-icing properties of metallic surfaces while offering an increased durability compared with currently used icephobic coatings.

Acknowledgements

The research work is conducted within the framework of European Commission H2020 project 'High-impact injection moulding platform for mass-production of 3D and/or large micro-structured surfaces with antimicrobial, self-cleaning, anti-scratch, anti-squeak and aesthetic functionalities" (HIMALAIA) and the UKIERI-DST programme on 'Surface functionalisation for food, packaging, and healthcare applications'. The authors would like to acknowledge the support provided by the EPSRC National Facility for X-Ray Photoelectron Spectroscopy at the Harwell Campus, UK, for conducting the XPS analysis.

References

1. Latthe, S.S., Sutar, R.S., Bhosale, A.K., Nagappan, S., Ha, C.S., Sadasivuni, K.K., Liu, S. and Xing, R., 2019. Recent developments in air-trapped superhydrophobic and liquid-infused slippery surfaces for anti-icing application. *Progress in Organic Coatings*, *137*, p.105373.
2. Malik, A.N., Khan, S.A. and Lazoglu, I., 2020. A novel hybrid frost detection and defrosting system for domestic refrigerators. *International Journal of Refrigeration*, *117*, pp.256-268.
3. Zhao, R., Huang, D., Peng, X. and Qiao, L., 2020. Comprehensive measures to enhance electric heater defrosting (EHD) performance for household frost-free refrigerators. *International Journal of Refrigeration*, *111*, pp.1-8.
4. Chavan, S., Foulkes, T., Gurumukhi, Y., Boyina, K., Rabbi, K.F. and Miljkovic, N., 2019. Pulse interfacial defrosting. *Applied Physics Letters*, *115*(7), p.071601.
5. Gaddam, A., Kattemalalawadi, B.S., Agrawal, A. and Joshi, S.S., 2017. Demarcating wetting states in textured microchannels under flow conditions by Poiseuille number. *Microfluidics and Nanofluidics*, *21*(8), p.137.
6. Pan, Q., Cao, Y., Xue, W., Zhu, D. and Liu, W., 2019. Picosecond laser-textured stainless steel superhydrophobic surface with an antibacterial adhesion property. *Langmuir*, *35*(35), pp.11414-11421.
7. Geyer, F., D'Acunzi, M., Sharifi-Aghili, A., Saal, A., Gao, N., Kaltbeitzel, A., Sloot, T.F., Berger, R., Butt, H.J. and Vollmer, D., 2020. When and how self-cleaning of superhydrophobic surfaces works. *Science advances*, *6*(3), p.eaaw9727.
8. Hou, W., Shen, Y., Tao, J., Xu, Y., Jiang, J., Chen, H. and Jia, Z., 2020. Anti-icing performance of the superhydrophobic surface with micro-cubic array structures fabricated by plasma etching. *Colloids and Surfaces A: Physicochemical and Engineering Aspects*, *586*, p.124180.
9. Bengaluru Subramanyam, S., Kondrashov, V., Rühe, J. and Varanasi, K.K., 2016. Low ice adhesion on nano-textured superhydrophobic surfaces under supersaturated conditions. *ACS applied materials & interfaces*, *8*(20), pp.12583-12587.
10. Shen, Y., Jin, M., Wu, X., Tao, J., Luo, X., Chen, H., Lu, Y. and Xie, Y., 2019. Understanding the frosting and defrosting mechanism on the superhydrophobic surfaces with multiscale structures for enhancing anti-frosting performance. *Applied Thermal Engineering*, *156*, pp.111-118.

11. Yue, X., Liu, W. and Wang, Y., 2018. Freezing delay, frost accumulation and droplets condensation properties of micro-or multiscalely-structured silicon surfaces. *International Journal of Heat and Mass Transfer*, *126*, pp.442-451.
12. Mohammadian, B., Annavarapu, R.K., Raiyan, A., Nemani, S.K., Kim, S., Wang, M. and Sojoudi, H., 2020. Delayed Frost Growth on Nanoporous Microstructured Surfaces Utilizing Jumping and Sweeping Condensates. *Langmuir*.
13. Yin, Z., Xue, M., Luo, Y., Hong, Z., Xie, C., Ren, Z. and Wang, H., 2020. Excellent static and dynamic anti-icing properties of multiscale structured ZnO superhydrophobic surface on Cu substrates. *Chemical Physics Letters*, p.137806.
14. Liu, G., Yuan, Y., Jiang, Z., Youdong, J. and Liang, W., 2020. Anti-frosting/anti-icing property of nano-ZnO superhydrophobic surface on Al alloy prepared by radio frequency magnetron sputtering. *Materials Research Express*, *7*(2), p.026401.
15. Zhang, Y., Klittich, M.R., Gao, M. and Dhinojwala, A., 2017. Delaying frost formation by controlling surface chemistry of carbon nanotube-coated steel surfaces. *ACS applied materials & interfaces*, *9*(7), pp.6512-6519.
16. Xi, N., Liu, Y., Zhang, X., Liu, N., Fu, H., Hang, Z., Yang, G., Chen, H. and Gao, W., 2018. Steady anti-icing coatings on weathering steel fabricated by HVOF spraying. *Applied Surface Science*, *444*, pp.757-762.
17. Barthwal, S. and Lim, S.H., 2019. Rapid fabrication of a dual-scale micro-nanostructured superhydrophobic aluminum surface with delayed condensation and ice formation properties. *Soft matter*, *15*(39), pp.7945-7955.
18. Belaud, C., Vercillo, V., Kolb, M. and Bonaccurso, E., 2020. Development of nanostructured icephobic aluminium oxide surfaces for aeronautic applications. *Surface and Coatings Technology*, p.126652.
19. Milles, S., Soldera, M., Voisiat, B. and Lasagni, A.F., 2019. Fabrication of superhydrophobic and ice-repellent surfaces on pure aluminium using single and multiscaled periodic textures. *Scientific Reports*, *9*(1), pp.1-13.
20. Long, J., He, Z., Zhou, C., Xie, X., Cao, Z., Zhou, P., Zhu, Y., Hong, W. and Zhou, Z., 2018. Multiscale micro-and nanostructures induced by nanosecond laser on copper for superhydrophobicity, ultralow water adhesion and frost resistance. *Materials & Design*, *155*, pp.185-193.
21. Long, J., He, Z., Zhou, P., Xie, X., Zhou, C., Hong, W. and Hu, W., 2018. Low-Cost fabrication of large-area broccoli-like multiscale micro-and nanostructures for metallic

super-hydrophobic surfaces with ultralow water adhesion and superior anti-frost ability. *Advanced Materials Interfaces*, *5*(13), p.1800353.

22. Boinovich, L.B., Emelyanenko, A.M., Emelyanenko, K.A. and Modin, E.B., 2019. Modus operandi of protective and anti-icing mechanisms underlying the design of longstanding outdoor icephobic coatings. *ACS nano*, *13*(4), pp.4335-4346.
23. Xing, W., Li, Z., Yang, H., Li, X., Wang, X. and Li, N., 2019. Anti-icing aluminum alloy surface with multi-level micro-nano textures constructed by picosecond laser. *Materials & Design*, *183*, p.108156.
24. Liu, Y., Zhang, Z., Hu, H., Hu, H., Samanta, A., Wang, Q. and Ding, H., 2019. An experimental study to characterize a surface treated with a novel laser surface texturing technique: Water repellency and reduced ice adhesion. *Surface and Coatings Technology*, *374*, pp.634-644.
25. Li, J., Zhou, Y., Wang, W., Xu, C. and Ren, L., 2020. Superhydrophobic copper surface textured by laser for delayed icing phenomenon. *Langmuir*, *36*(5), pp.1075-1082.
26. Volpe, A., Gaudiuso, C. and Ancona, A., 2020. Laser Fabrication of Anti-Icing Surfaces: A Review. *Materials*, *13*(24), p.5692.
27. Huang, C., Bell, R., Tsubaki, A., Zuhlke, C.A. and Alexander, D.R., 2018. Condensation and subsequent freezing delays as a result of using femtosecond laser functionalized surfaces. *Journal of Laser Applications*, *30*(1), p.011501.
28. Volpe, A., Gaudiuso, C., Venere, L.D., Licciulli, F., Giordano, F. and Ancona, A., 2020. Direct femtosecond laser fabrication of superhydrophobic aluminum alloy surfaces with anti-icing properties. *Coatings*, *10*(6), p.587.
29. Siddiquie, R.Y., Gaddam, A., Agrawal, A., Dimov, S.S. and Joshi, S.S., 2020. Anti-biofouling properties of femtosecond laser-induced submicron topographies on elastomeric surfaces. *Langmuir*, *36*(19), pp.5349-5358.
30. Karkantonis, T., Gaddam, A., See, T.L., Joshi, S.S. and Dimov, S., 2020. Femtosecond laser-induced sub-micron and multi-scale topographies for durable lubricant impregnated surfaces for food packaging applications. *Surface and Coatings Technology*, p.126166.
31. Jwad, T., Penchev, P., Nasrollahi, V. and Dimov, S., 2018. Laser induced ripples' gratings with angular periodicity for fabrication of diffraction holograms. *Applied Surface Science*, *453*, pp.449-456.
32. Vercillo, V., Tonnicchia, S., Romano, J.M., García-Girón, A., Aguilar-Morales, A.I., Alamri, S., Dimov, S.S., Kunze, T., Lasagni, A.F. and Bonaccurso, E., 2020. Design Rules

for Laser-Treated Icephobic Metallic Surfaces for Aeronautic Applications. *Advanced Functional Materials*, *30*(16), p.1910268.

33. Wang, G. and Guo, Z., 2019. Liquid infused surfaces with anti-icing properties. *Nanoscale*, *11*(47), pp.22615-22635.
34. Samanta, A., Wang, Q., Shaw, S.K. and Ding, H., 2020. Roles of chemistry modification for laser textured metal alloys to achieve extreme surface wetting behaviors. *Materials & Design*, p.108744.
35. Joshipura, I.D., Ayers, H.R., Castillo, G.A., Ladd, C., Tabor, C.E., Adams, J.J. and Dickey, M.D., 2018. Patterning and reversible actuation of liquid gallium alloys by preventing adhesion on rough surfaces. *ACS applied materials & interfaces*, *10*(51), pp.44686-44695.
36. Garcia-Giron, A., Romano, J.M., Batal, A., Dashtbozorg, B., Dong, H., Solanas, E.M., Angos, D.U., Walker, M., Penchev, P. and Dimov, S.S., 2019. Durability and wear resistance of laser-textured hardened stainless steel surfaces with hydrophobic properties. *Langmuir*, *35*(15), pp.5353-5363.
37. Kietzig, A.M., Hatzikiriakos, S.G. and Englezos, P., 2009. Patterned superhydrophobic metallic surfaces. *Langmuir*, *25*(8), pp.4821-4827.
38. Varughese, S.M. and Bhandaru, N., 2020. Durability of submerged hydrophobic surfaces. *Soft Matter*, *16*(6), pp.1692-1701.
39. Giannuzzi, G., Gaudiuso, C., Di Mundo, R., Mirenghi, L., Fraggelakis, F., Kling, R., Lugarà, P.M. and Ancona, A., 2019. Short and long term surface chemistry and wetting behaviour of stainless steel with 1D and 2D periodic structures induced by bursts of femtosecond laser pulses. *Applied Surface Science*, *494*, pp.1055-1065.
40. Wu, H., Yang, Z., Cao, B., Zhang, Z., Zhu, K., Wu, B., Jiang, S. and Chai, G., 2017. Wetting and dewetting transitions on submerged superhydrophobic surfaces with hierarchical structures. *Langmuir*, *33*(1), pp.407-416.
41. Tang, W., Liu, L., Ruan, Q., Wu, Z., Yang, C., Cui, S., Ma, Z., Fu, R.K., Tian, X., Chu, P.K. and Wu, Z., 2020. Dynamic changes of hydrophobic behavior during icing. *Surface and Coatings Technology*, p.126043.
42. Lengaigne, J., Bousser, E., Brown, S., Xing, P., Turcot, F., Dolatabadi, A., Martinu, L. and Klemberg-Sapieha, J.E., 2020. In situ ice growth kinetics on water-repellent coatings under atmospheric icing conditions. *Surface and Coatings Technology*, *399*, p.126136.
43. Pham, Q.N., Zhang, S., Montazeri, K. and Won, Y., 2018. Droplets on Slippery Lubricant-Infused Porous Surfaces: A Macroscale to Nanoscale Perspective. *Langmuir*, *34*(47), pp.14439-14447.

44. Mohammadian, B., Annavarapu, R.K., Raiyan, A., Nemani, S.K., Kim, S., Wang, M. and Sojoudi, H., 2020. Delayed Frost Growth on Nanoporous Microstructured Surfaces Utilizing Jumping and Sweeping Condensates. *Langmuir*.
45. Wong, W.S., Hegner, K.I., Donadei, V., Hauer, L., Naga, A. and Vollmer, D., 2020. Capillary Balancing: Designing Frost-Resistant Lubricant-Infused Surfaces. *Nano Letters*.
46. Azouz, R.A. and Korany, R.M., 2020. Toxic Impacts of Amorphous Silica Nanoparticles on Liver and Kidney of Male Adult Rats: an In Vivo Study. *Biological Trace Element Research*, pp.1-10.

Supplementary information

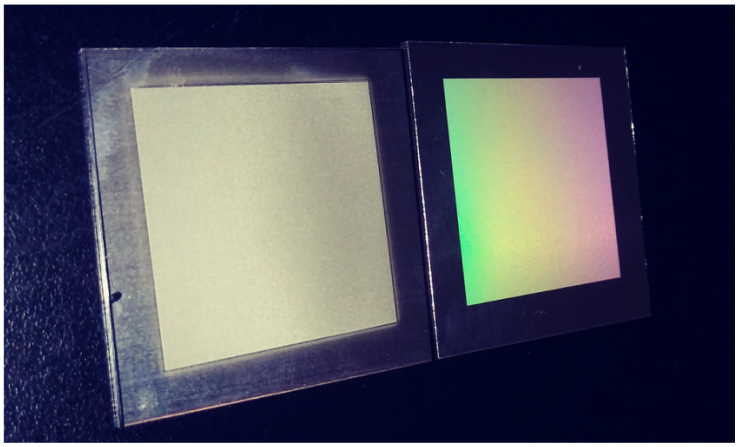

Figure S1: Optical images of femtosecond laser-induced multiscale (left) and LIPSS (right) topographies on SS. Processed area is 30 mm x 30 mm.

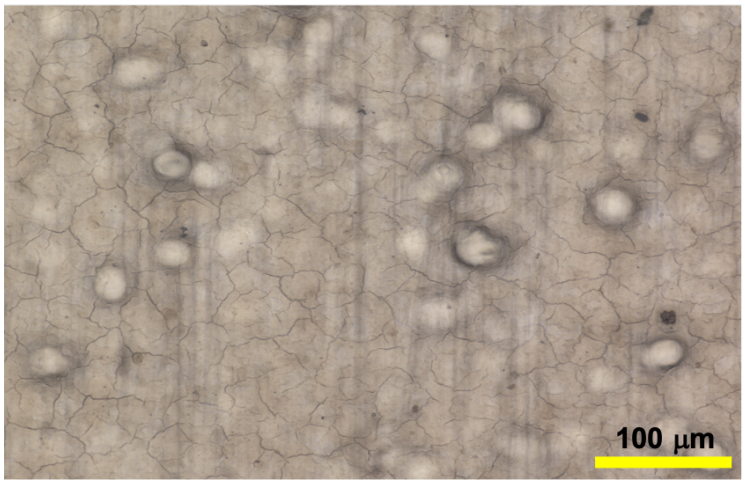

Figure S2: Optical micrograph of the NeverWet® coating on a SS surface.

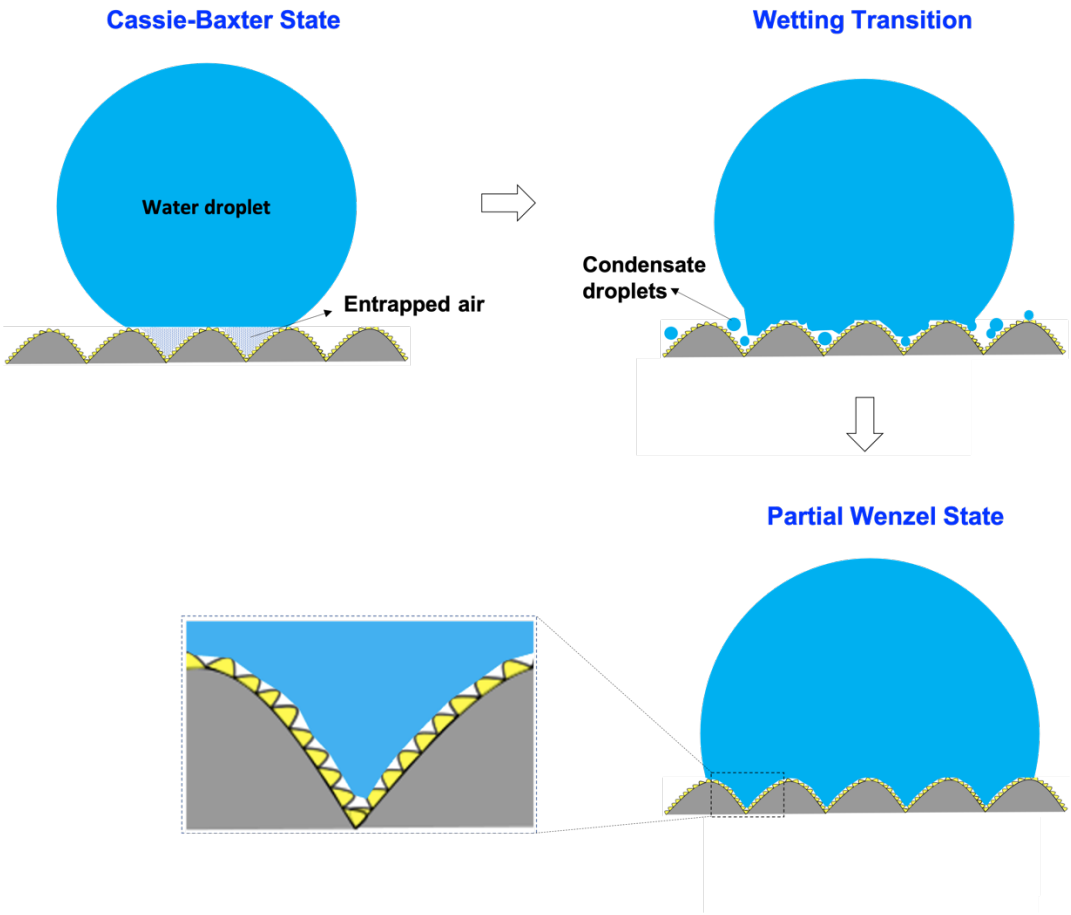

Figure S3: Condensation-driven wetting transition on surfaces with multiscale topography.

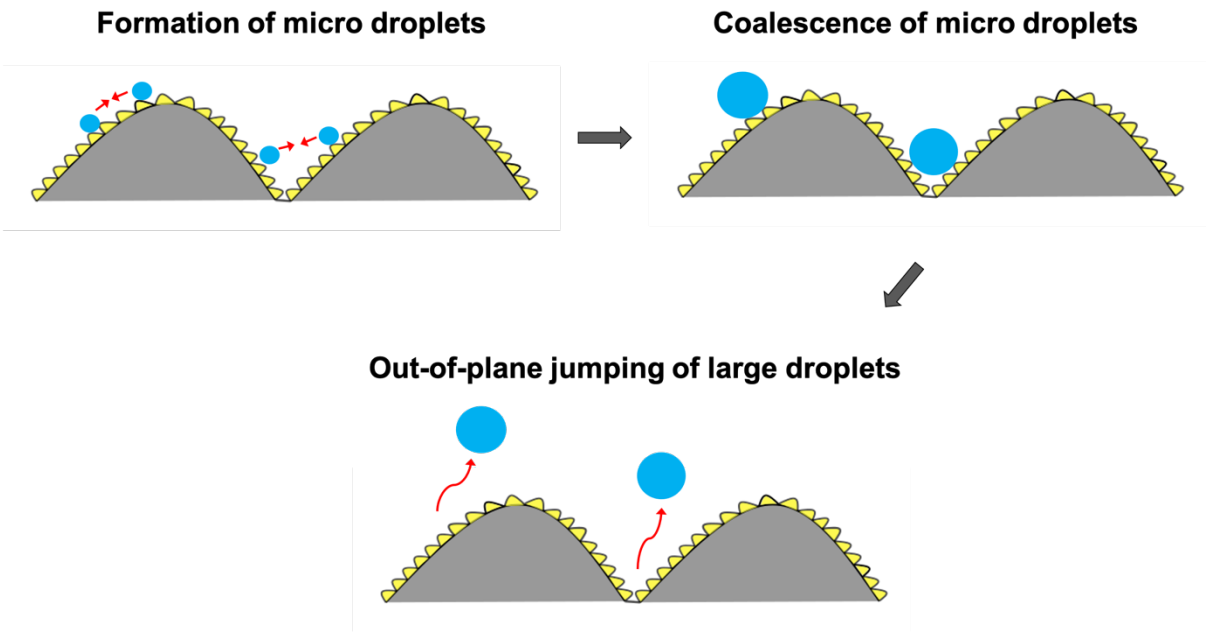

(a)

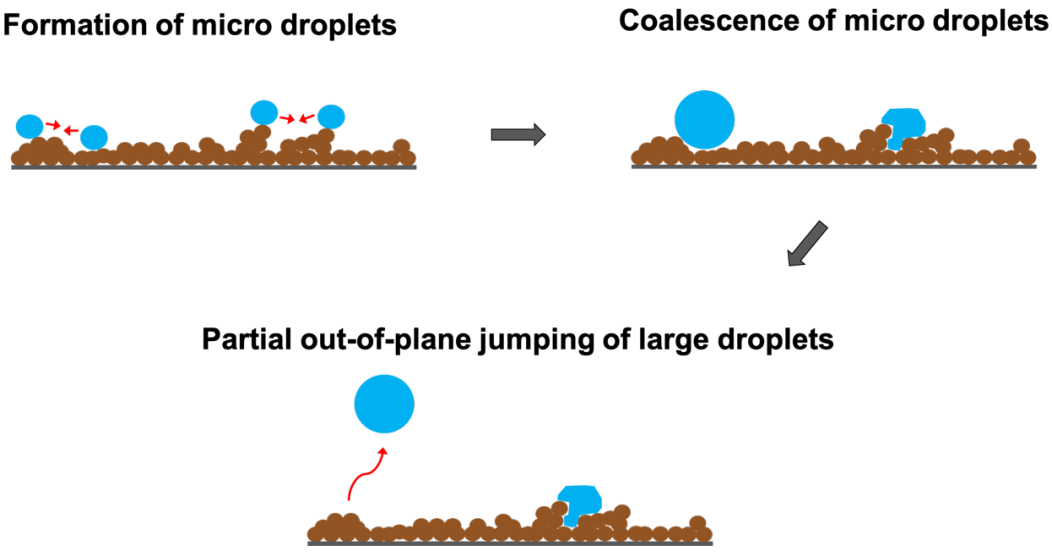

(b)

Figure S4: Out-of-plane jumping of droplets on **(a)** Multiscale and **(b)** NeverWet surfaces.

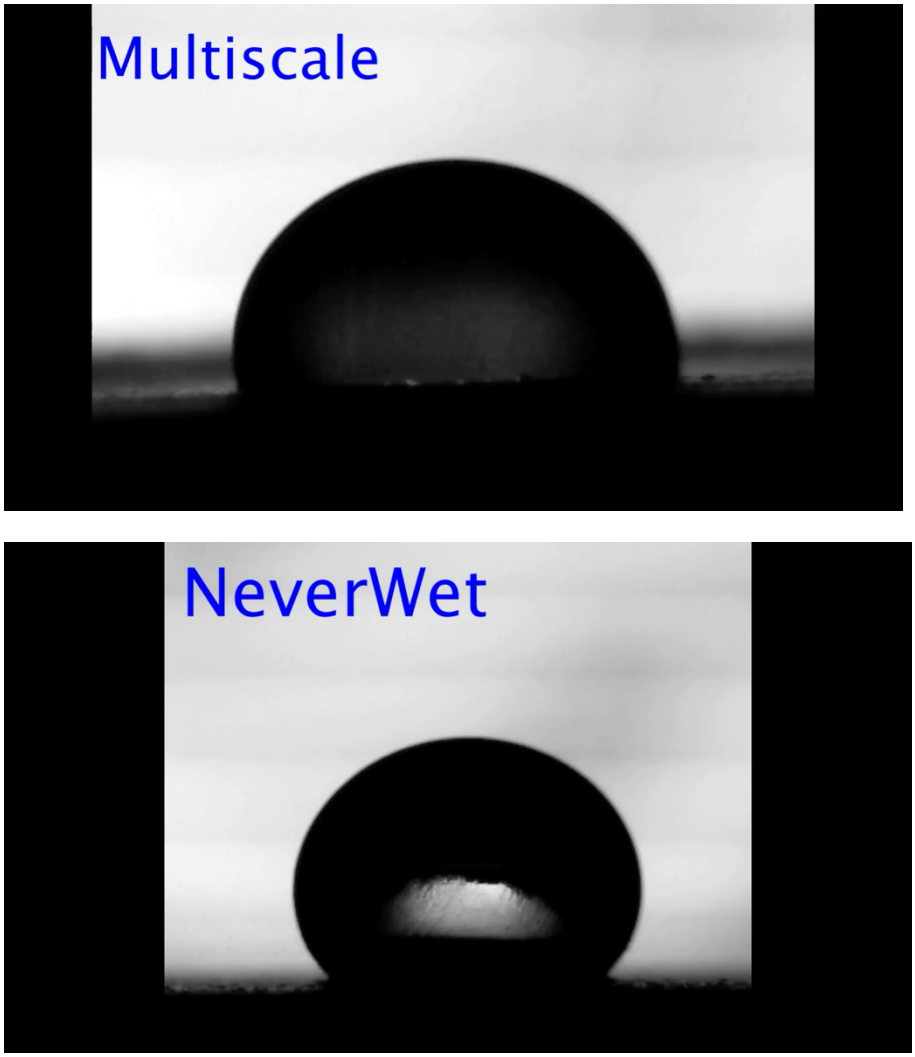

Video S1: Isothermal freezing process of a sessile droplet on MS and NW surfaces

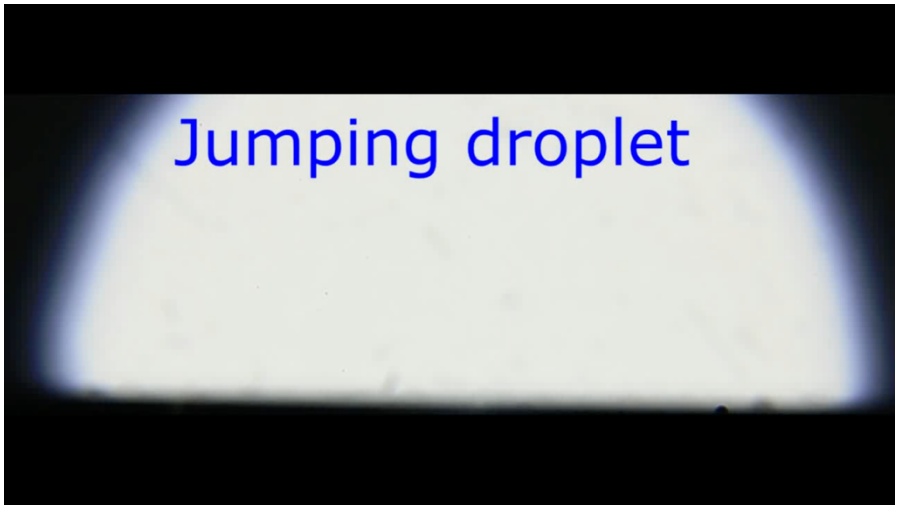

Video S2: Jumping droplet phenomena on a surface with MS topography